A high-sensitivity high-resolution intravascular photoacoustic catheter through mode cleaning in a graded-index fiber

Yuhao Yuan [a],[1], Guangju Zhang [a],[*],[1], Yuqi Chen [b], Hongli Ni [a], Mingsheng Li [a], Michael Sturek [c],[2], Ji-Xin Cheng [a],[b],[**]

[a] Department of Electrical and Computer Engineering, Boston University, Boston, MA 02215, USA
[b] Department of Biomedical Engineering, Boston University, Boston, MA 02215, USA
[c] CorVus Biomedical, LLC and CorVus Foundation, Inc, Crawfordsville, IN 47933, USA

ARTICLE INFO

ABSTRACT

Intravascular photoacoustic imaging has been developed to evaluate the possibility of plaque rupture in atherosclerosis by high spatial resolution imaging of lipid. However, the detection sensitivity and spatial resolution are compromised by the poor focusing caused by a multimode fiber. In this work, we report an intravascular photoacoustic catheter with mode self-cleaning in a graded-index fiber to improve the beam quality and the sensitivity for lipid detection. Compared with the higher-order modes in a step-index multimode fiber, the lower-order modes generated by the self-cleaning effect in the graded-index fiber greatly enhanced the photoacoustic spatial resolution and detection sensitivity. The dominant ringing artifact caused by laser absorption of the ultrasound transducer was further reduced by using stripe suppression. A lipid plaque mimicking phantom was imaged for evaluation. Lipid particles with a small diameter of 75.7 μm were clearly observed.

1. Introduction

To date, atherosclerosis has an increasing morbidity and is affecting younger people [1]. Plaques consisting of lipid and other substances are built up inside the artery walls in atherosclerosis, ultimately blocking the blood flow. Another adverse event is the rupture of lipid-laden plaque in atherosclerosis, which is the major cause of acute coronary syndrome [2]. Generally, the plaque is not fully reversible once being formed [3,4]. Yet, not all the plaques require coronary interventions like angioplasty or stenting [5]. Reducing the lipid accumulation and inflammation pharmacologically is a key strategy in conservative treatment [5–9]. To determine the need for vascular intervention, the plaque vulnerability, featured by a thinning fibrous cap and enlarged lipid necrotic core, is estimated by its size and location inside an artery wall [10]. Angiography is the most common method to image an artery with significant stenosis [11]. Intravascular ultrasound (IVUS) imaging has greater spatial resolution to evaluate much smaller plaque at a resolution of 100–200 μm [12]. Intravascular optical coherence tomography enables finer details at 10–20 μm [13]. However, chemical information, especially that of lipid, are not resolved by the modalities mentioned above. Infrared spectroscopy offers lipid abundance information, yet without the information about location and size [14,15]. Fluorescence lifetime imaging is coupled with IVUS to provide molecular information, whereas the imaging depth is sacrificed [16].

Intravascular photoacoustic (IVPA) catheters have been developed to probe lipid-laden plaques in atherosclerosis [17–27]. The first overtone of C-H stretch vibration at around 1730 nm has been used for selective imaging of lipids [28–31]. The lipid size and location information could be acquired based on the overtone vibrational absorption and photoacoustic effect, while the anatomy of the artery is imaged at the same time by IVUS on the catheter. Molecular labeling with nanoprobes provide extra information of inflammation and angiogenesis [32,33]. Both single mode and multimode fibers have been used in IVPA catheter design. To improve the spatial resolution, a single mode fiber was employed to output optical-diffraction limited resolution of about 19.6 μm [34]. However, the damage threshold of a single mode fiber is much

lower than that of a multimode fiber because of the smaller mode field diameter, which limits the sensitivity for small lipid detection. A tapered fiber was adopted to improve the laser coupling efficiency, where the power was several times greater than in single mode fibers, while keeping a fine resolution of 18 μm [35]. Yet, the tapered fiber is prone to rapid degradation after fabrication majorly due to the dust deposited on the surface [36]. Careful fabrication and assembling in dust-free environment may prevent the degradation over a week [36]. However, the demanding requirement may limit the further application of tapered fiber, especially when the fiber is in contact with the surrounding environment. IVPA catheters assembled with step-index multimode fiber allow high coupled laser power because of the larger effective area compared with single mode fiber, and eventually improve the signal by increasing the pulse energy [37,38]. However, the lateral resolution is poor because of the speckled illumination caused by the randomization of light propagation in multimode fibers. Moreover, the sensitivity for lipid detection using a step-index multimode fiber is compromised due to the distorted laser profile in higher-order modes (HOMs).

Mode cleaning has been applied to improve the beam quality usually using spatial filters to reject light propagation modes other than the fundamental mode (FM). Yet considerable laser energy is reserved in HOMs in multimode fibers. And it is also impractical to spatially filter the laser in the tiny catheter. An elegant way of creating a high-energy Gaussian beam is through mode cleaning inside a graded-index (GRIN) multimode fiber [39]. A self-cleaning occurs in the GRIN fiber and could be explained by the quasi phase matching in the periodic longitudinal modulation of refractive index caused by periodic spatial self-imaging and Kerr nonlinearity, where a higher nonlinear loss occurs in HOMs compared to that in the FM or lower-order modes (LOMs), resulting in an energy transfer from HOMs to FM/LOMs [39]. In other words, the randomization of light propagation in multimode fiber is reduced and a tight focus could be achieved in a GRIN fiber with high input energy beyond the threshold of Kerr nonlinearity. Previously, our team reported an IVPA catheter using the spatial beam self-cleaning effect in a GRIN multimode fiber, in which a spatial lateral resolution of 30 μm was achieved [40], due to the formation of a tight focus with a

quasi-Gaussian beam from the GRIN fiber [39]. However, high-sensitivity detection of lipids using this approach has not been achieved. In addition, performance of GRIN fiber in IVPA imaging remains to be explored, since the initial condition of the input beam, including angle of launch, excitation radial position and phase front, may lead to different transverse modes of the output laser [41].

Here, we report a high-sensitivity high-spatial-resolution intravascular photoacoustic catheter through mode self-cleaning in a graded-index multimode fiber. We use a nanosecond laser at 1731 nm for excitation of the first overtone of C-H stretch vibration. A plaque-mimicking phantom is imaged to evaluate the performance of our system. We compare the performance of LOMs and HOMs after a GRIN fiber for sensing lipids with a 10 MHz ultrasound transducer. The signal to noise ratio (SNR) is much improved by employing the mode self-cleaning effect. We also find that the ringing artifacts could not be simply removed using bandpass filters, resulting in a disruptive interpretation of the images. Alternatively, the circular ringing artifacts are found to be stripes in cartesian coordinates and could be removed with a stripe filter easily. Altogether, imaging of lipids as small as 75.7 μm in a phantom is achieved.

2. Material and methods

2.1. IVPA imaging system

The schematic of the system is shown in Fig. 1. A 1731 nm laser (Photonics Industries) with a pulse duration of 10 ns and a tunable repetition rate from 2 kHz to 10 kHz was used for the excitation of C-H bonds. The laser was first attenuated with ND filters and then coupled to a GRIN fiber (2002–200, Berkshire Photonics). Generally, to build an IVPA catheter, the fiber should be incorporated into a slip ring and rotary joint with intermediate fibers for rapid spinning. In our case, the self-cleaning effect of the GRIN fiber is quite sensitive to the initial condition at the input and a relative stable fiber coupling structure was adopted. Therefore, only one single GRIN fiber was used, with one end fixed at the fiber coupler and the other end passed through the slip ring
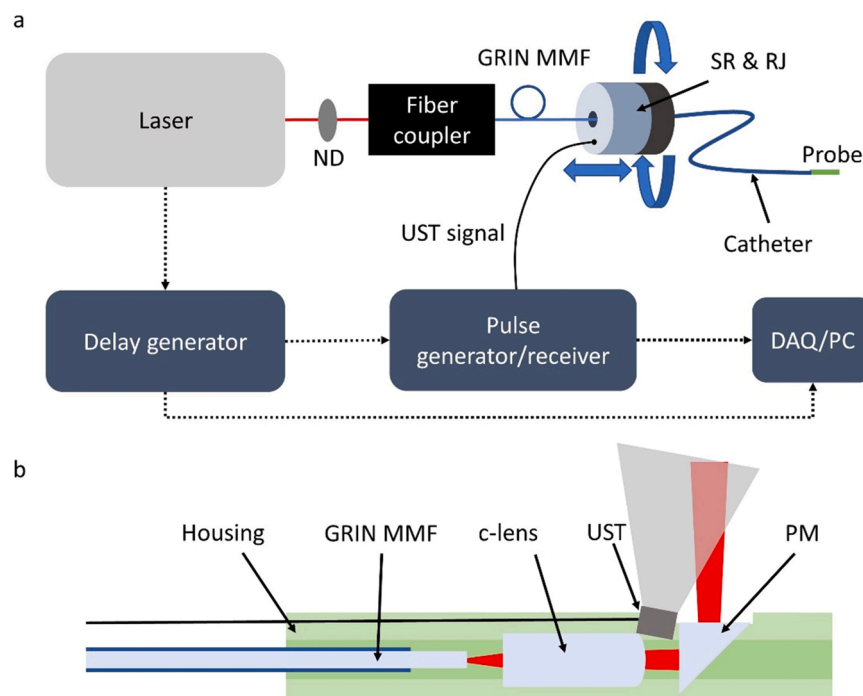

Fig. 1. Schematic of the IVPA imaging system (a) and the IVPA probe (b). The gray area above the UST showed the detection area of acoustic wave. ND: neutral density filter; GRIN MMF: graded-index multimode fiber; SR: slip ring; RJ: rotary joint; UST: ultrasound transducer; DAQ/PC: data acquisition card / personal computer; PM: prism mirror.

and rotary joint as indicated in a previous study [40]. To minimize the mode changing and the damage to the fiber caused by over twisting, the direction of rotation was reversed every revolution. A c-lens (customized, diameter 0.5×1.0 mm, R1.0, AR 1725 ± 30 nm) was used to collimate the laser at the free end of the fiber in a 3D printed housing tube. The laser was reflected at 90° with a prism mirror (#66–772, Edmund optics) to allow side illumination on the tissue. According to our previous study, the PA signal from lipids is centered at around 10 MHz [24]. Hence, a 10 MHz ultrasound transducer (sensing area 0.45 $*0.45$ mm^2, 0.5 mm thick, AT34603, Blatek Inc.) was mounted on the tube with a tilted angle of 10 degrees for lipid detection [40]. The tilted angle was determined by the acceptance angle of the transducer and the distance between the laser output and the transducer. Noting that the acceptance angle of MHz Piezoelectric transducers is within ± 20 degrees [24], the detection area of the ultrasound transducer was illustrated in Fig. 1b. Acoustic signals at a distance greater than 0.5 mm from the probe could be detected by the tilted transducer. The outer diameter of the IVPA probe was about 1.7 mm. In order to compare the PA signal generated by LOMs and HOMs, the initial condition at the fixed end of the fiber was optimized to output LOMs, then the fiber coupler was rotated by 90°, which could change the output transverse mode from LOMs to HOMs. In all cases, the output modes were confirmed by an IR camera and a power meter. The power used for phantom imaging was about 0.11 J/cm^2 on the sample, which was lower than the ANSI safety standard 1.0 J/cm^2 for skin at 1.7 μm. The PA signal detection was synchronized with the laser and was amplified by a factor of 39 dB via a pulser/receiver (5073PR, Olympus). A data acquisition card (ATS9350, AlazarTech) with a sampling rate of 500 MHz was used. A LabView program was designed for co-registered IVPA/IVUS imaging.

2.2. Lipid-laden plaque mimicking phantom

A lipid-rich phantom was prepared to mimic the lipid plaque burdened artery. Agarose gel (1% w/w) in water was warmed and mixed with ground palmitic acid powder (Sigma) gently without making air bubbles. Palmitic acid has a melting temperature at 62.9° Celsius and can keep its shape before the gelling of agarose solution. The mixture was poured into a cylindrical tube having an inner diameter of 9 mm. To form the lumen, a 3-mm diameter stick was inserted into the center of the tube. The phantom was cooled down to room temperature prior to imaging.

2.3. Stripe suppression filter

The raw PA signals before Hilbert transform were displayed as a 2D image in which each row represented an A-line at a specific angle and each column represented the time of flight. The stripe suppression filter in ImageJ was applied to suppress the vertical stripes with 0% tolerance of direction [42].

3. Results

To demonstrate mode cleaning, we measured the laser profile with an IR camera after the GRIN fiber (Fig. 2a). The initial condition at the input of the GRIN fiber was optimized to output a tight laser spot by adjusting the incident angle and distance between the fiber and fiber coupler. Low input laser energy (10 μJ/pulse before the GRIN fiber) did not display prominent mode cleaning, in which an irregular beam shape could be observed (Fig. 2b). By increasing the laser energy to 100 μJ/pulse, the laser spot was gradually confined in the center and displayed a quasi-Gaussian shape (Fig. 2c), demonstrating the self-cleaning effect. The GRIN fiber was then coupled into the IVPA probe and the laser profile was measured (Fig. 2d). A Gaussian-like beam profile was shown, in which most of the laser power was concentrated (Fig. 2e). In contrast, a speckled energy distribution was observed in HOMs at the same location when the initial condition at the input for LOMs was slightly disrupted by rotating the fixed end of the fiber by 90° (Fig. 2f). A much greater diameter of the illumination area was displayed in HOMs,
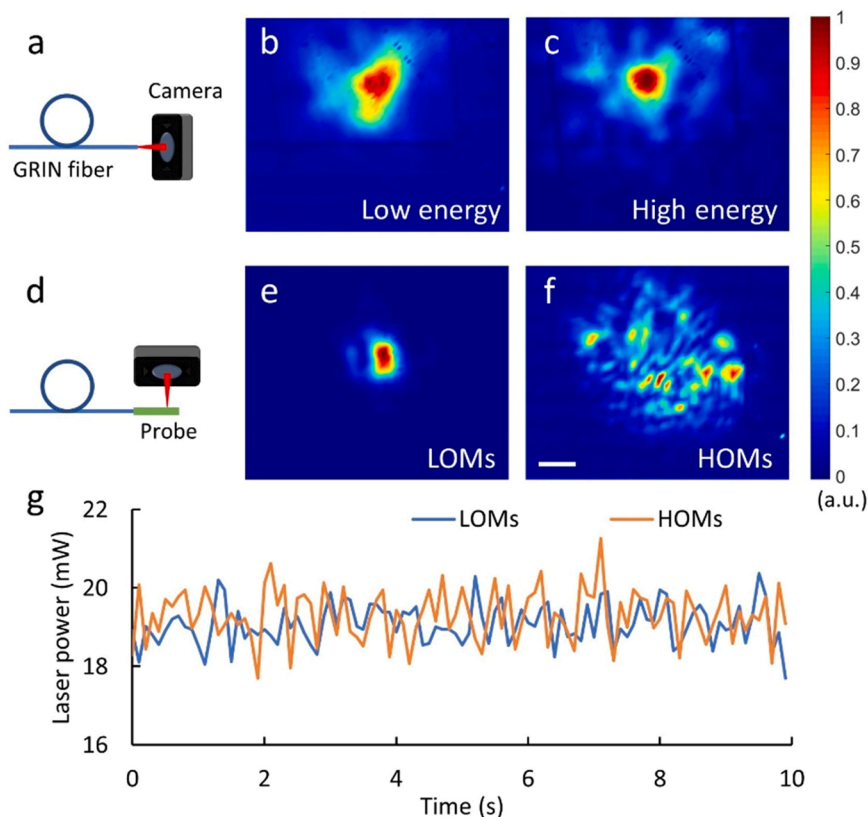

Fig. 2. Laser mode self-cleaning in a GRIN multimode fiber. (a) The laser profile measurement setup for (b) and (c) by placing the camera at about 3 cm from the output. The laser beam profile was confined to a quasi-Gaussian power distribution when the laser energy increased from 10 μJ/pulse (b) to 100 μJ/pulse (c). (d) The laser profile measurement setup for (e) and (f) by placing the camera at about 5 cm from the output. (e) A tight focus with LOMs was found after the IVPA probe. (f) A speckled power distribution with HOMs by slightly modifying the initial condition for LOMs. Scale bar: 1 mm. (g) The total laser power remained the same level when the mode was switched from LOM to HOM.

consistent with previous studies [39,43]. According to $P_0 = \Gamma\Phi\mu_a$, where P_0 is the initial pressure, Γ is the Grüneisen parameter, Φ is the incident fluence, and μ_a is the optical absorption coefficient [44], the incident fluence in HOMs is relatively smaller than that in LOMs, leading to a weaker PA signal and a poorer spatial resolution, which typically happens in step-index multimode fibers [39]. Although the laser energy was redistributed, no significant difference in total laser power was observed by switching from LOMs to HOMs (Fig. 2g). We further measured the robustness of the mode self-cleaning by twisting the GRIN fiber. Although being hard to achieve a constant FM output with a 4-m-long GRIN fiber as described in a previous study [41], a relatively tight laser spot could be maintained in LOMs (supplementary movie 1) while a speckle pattern was constantly found in HOMs (supplementary movie 2).

Supplementary material related to this article can be found online at doi:10.1016/j.pacs.2023.100451.

A phantom that mimicked lipid plaque burdened artery was imaged with both LOMs and HOMs at the same laser power (Fig. 3). Under each condition, 64 images were averaged. A higher contrast and lower noise were observed in IVPA images by LOMs compared with that by HOMs (Fig. 3a & b). However, ringing artifact, which was a result of laser interacting with the ultrasound transducer, was dominant in both LOMs and HOMs, leading to a broad background and compromising the sensitivity of real lipid signal [29]. To be specific, the intensity of ringing artifacts by LOMs were stronger than that by HOMs because of the higher energy density, which turned out leading to a relatively poorer imaging contrast in the raw images by LOMs. To address that, two bandpass filters, 5–25 MHz and 10–20 MHz, were applied to the images to reduce the artifacts as well as the noise during the data collection, respectively (Fig. 3c-f). The ringing artifacts were more strongly suppressed by the narrower 10–20 MHz filter than by the 5–25 MHz filter. The weaker lipid signal could be identified clearly with more details after 10–20 MHz bandpass filtering in both LOMs and HOMs.

To quantify the performance of LOMs and HOMs, representative A-lines at the same location of the phantom, as marked along the yellow dotted line in Fig. 3a, were compared (Fig. 4). The SNR by LOMs was found to be 3.3 times greater than that by HOMs without using any filters, in which the SNR by LOMs was 62.6 with a peak intensity value of 356.2 while the SNR by HOMs was 18.9 with a peak intensity value of 88.8 (Fig. 4a & b). But the signal intensities were partially contributed by the ringing artifacts. Thus, the SNR was recalculated by subtracting the average ringing artifact signal at the same depth of the phantom. The corrected SNR by LOMs was 45.2 with a peak intensity value of 257 and the corrected SNR by HOMs was 19.9 with a peak intensity value of 93.4, leading to a corrected SNR by LOMs 2.3 times greater than that by HOMs. With 5–25 MHz filters, smooth A-lines were achieved but the ringing artifacts remained distinctly present in both LOMs and HOMs (Fig. 4c & d). A stronger suppression of ringing artifacts was observed with narrower 10–20 MHz bandpass filters (Fig. 4e & f). Although the ringing artifacts were reduced by the bandpass filters, the lipid signals were compromised as well and the ringing artifact remained strongly obscuring the possibly weak lipid signal, especially in a closer region to the ultrasound transducer.

To further improve the imaging quality, we suppressed the ringing artifacts on the unfiltered images with a stripe suppression filter that removed the artifacts spatially among A-lines while the aforementioned bandpass filters removed the noise during data collection in the time domain (Fig. 5a, Figs. S1 & S2). Bandpass filters were also applied after removing the ringing artifacts by the stripe suppression filter (Fig. 5b & c). The ringing artifacts were significantly reduced in comparison to the images without stripe suppression. The same A-line as shown in Fig. 4 was analyzed. We isolated the ringing artifacts and found that the target lipid signal was indeed mixed with the artifact background (Fig. 5d and Fig. S3). Unlike the bandpass filters, the stripe filter did not compromise the SNR and signal intensity of the lipid (Fig. 5e and Fig. S3). The ringing artifacts showed overlapping frequency with the lipid signal, making the bandpass filters less efficient (Fig. S1). A small lipid plaque (red box in Fig. 5a) could be clearly identified after removing the ringing artifacts in LOMs. The FWHM of the smallest lipid particle was 75.7 μm, measured at 1.9 mm from the transducer, indicating that high-sensitivity and high-
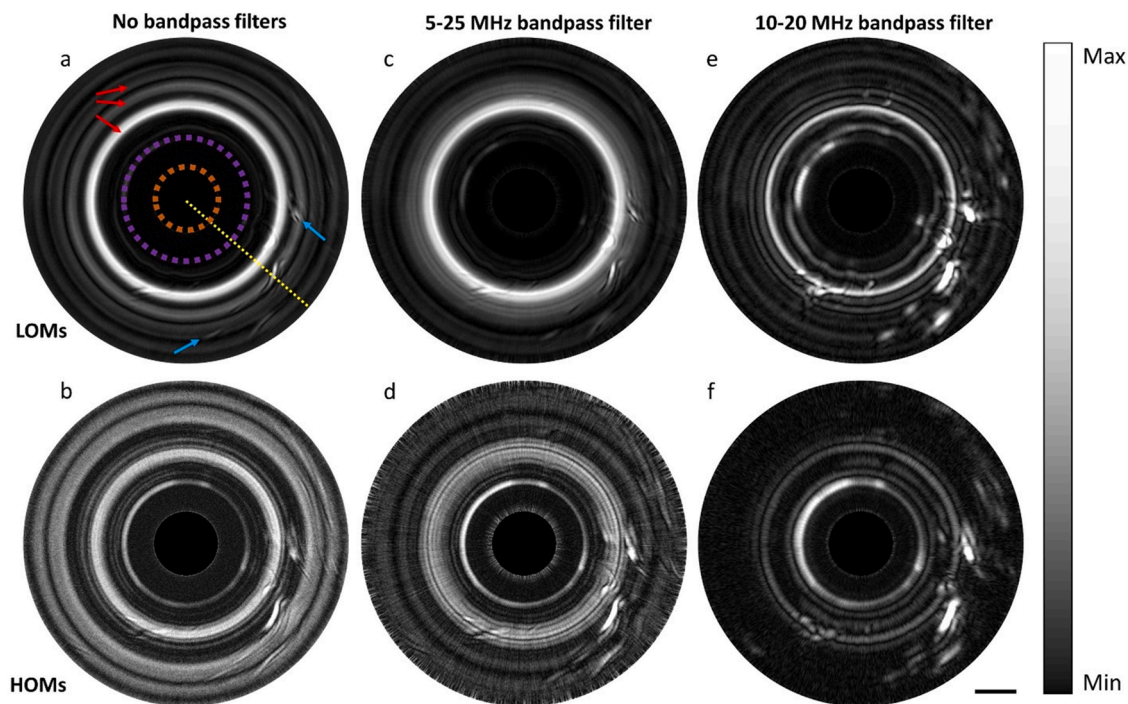

Fig. 3. IVPA images of the same location in a lipid plaque mimicking phantom. Laser in LOMs was used in (a), (c), (e), while laser in HOMs was used in (b), (d), and (f). No bandpass filters were applied in (a) and (b), in which dominant ringing artifacts (red arrows) were observed and the lipid signals (blue arrows) were concealed in the background. The probe was marked in the orange dotted line and the lumen of the phantom was marked in the purple dotted line. The yellow dotted line was analyzed in Fig. 4. A 5–25 MHz bandpass filter was applied in (c) and (d). A 10–20 MHz bandpass filter was applied in (e) and (f). Scale bar: 1 mm.
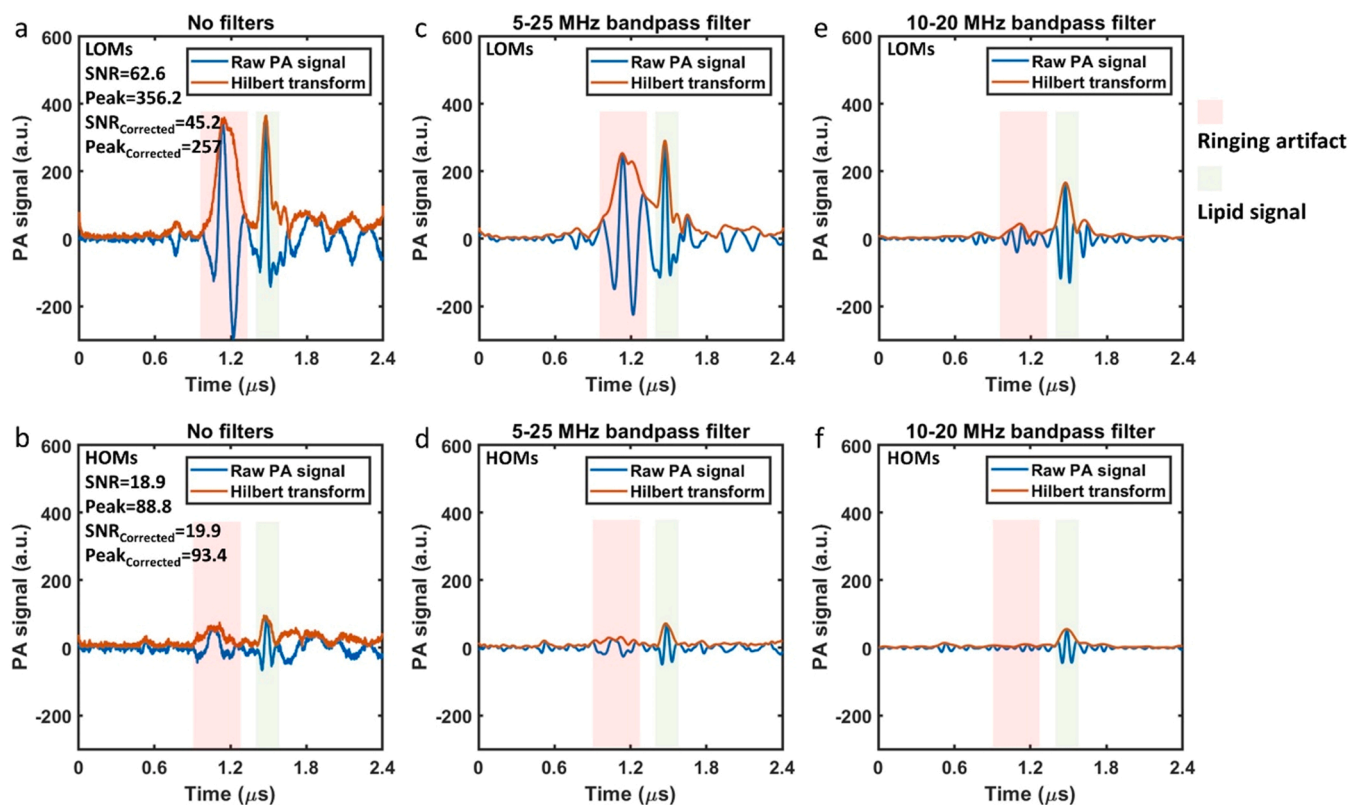
Fig. 4. Representative A-lines (along the yellow dotted line in Fig. 3a) of ringing artifact (red) and lipid signal (green). A-lines in LOMs and HOMs were from the same location. Laser in LOMs was used in (a),(c), (e), while laser in HOMs was used in (b), (d), and (f). No bandpass filters were applied in (a) and (b). A 5–25 MHz bandpass filter was applied in (c) and (d). A 10–20 MHz bandpass filter was applied in (e) and (f).

spatial-resolution lipid detection could be achieved.

4. Discussion

While IVPA imaging of lipids using a laser at 1.7 μm has been well illustrated, the speckle pattern from a multimode fiber not only compromises the spatial resolution, but also limits the sensitivity of detecting small lipid particles due to a broad distribution of the laser energy. In this work, we employed the mode self-cleaning effect in a GRIN fiber [40] and generated a tightly focused laser profile at a wavelength of 1731 nm. A high-sensitivity and high-spatial-resolution IVPA imaging system was demonstrated and label-free imaging of a lipid plaque mimicking phantom was performed. We detected a lipid particle with a diameter of about 75.7 μm at 1.9 mm from the transducer with a relatively low laser energy of 5 μJ per pulse.

With a higher input energy, the GRIN fiber displayed a prominent self-cleaning effect that outputs a quasi-Gaussian beam. Yet, we also found that the initial condition of the laser could affect the performance of the GRIN fiber. By rotating the fiber coupler, the laser profile changed dramatically, while the total laser power remained the same. What's more, when the fiber was twisted or bent with a small radius, the laser profile changed as well. In this work, we did not achieve a constant fundamental mode during fiber rotation. It could be due to (1) the imperfect initial condition at the fiber coupler; (2) disturbance of internal reflection during fiber twisting/bending; or (3) failing to meet the threshold of nonlinear non-reciprocity in terms of laser power. Nevertheless, most of the energy remained in a certain center area in LOMs during fiber twisting/bending. Although it is hard to tell if an optimal initial condition has been achieved, it's still possible to improve the self-cleaning by (1) using a longer GRIN fiber as the highly multimodal distribution is gradually collapse into bell-shape transverse profile; (2) using a higher pulse energy to increase the Kerr nonlinear index so a

short fiber would be enough; or (3) minimizing the bending or twisting of the fiber with a stiffer torque coil to hold the fiber in position.

Compared with HOMs, a higher SNR was achieved in LOMs because the quasi-Gaussian laser profile allowed tighter optical focusing. In our experiments, we simply used a c-lens to collimate the laser beam. To further improve sensitivity and spatial resolution, lenses with shorter focal length could be used.

We also noticed a low coupling efficiency in the catheter. A pulse energy of 100 μJ was sent to the fiber coupler for IVPA imaging but only 5 μJ was retained at the output of the probe. We observed a ~10% energy loss at the fiber coupler that could be because of the coating issue. Most of the energy was lost inside the probe. That was because the probe was not capsulated, and water was in contact with all the optical components. Noting that the water absorption coefficient is 6.44 cm^{-1} at 1730 nm, only about 30% of the energy could reach the prism mirror due to presence of water in the probe. What's more, only a small portion of light could be reflected by the prism mirror with a water interface. A low transmission was reached as a consequence. Such an issue could be further significantly improved by using a cap to enclose the optical parts. As performing in the blood vessels, water absorption is one of the major challenges for IVPA imaging at 1.7 μm. Fortunately, the GRIN fiber allows high pulse energy to be delivered to the target, which provides enough energy to generate PA signal even in a larger vessel with greater water absorption.

A dominant ringing artifact was observed during IVPA imaging. Such artifact was caused by laser absorption by the ultrasound transducer and was dependent on the laser modes. The 10 MHz transducer had a relatively larger size (0.45 *0.45 *0.5 mm^3) than higher frequency transducers, leading to a higher chance for the stray laser reaching the transducer. A bandpass filter was applied to the A-lines to remove the noise that was generated during data collection, whereas the ringing artifact showed up constantly even in the presence of bandpass filters.
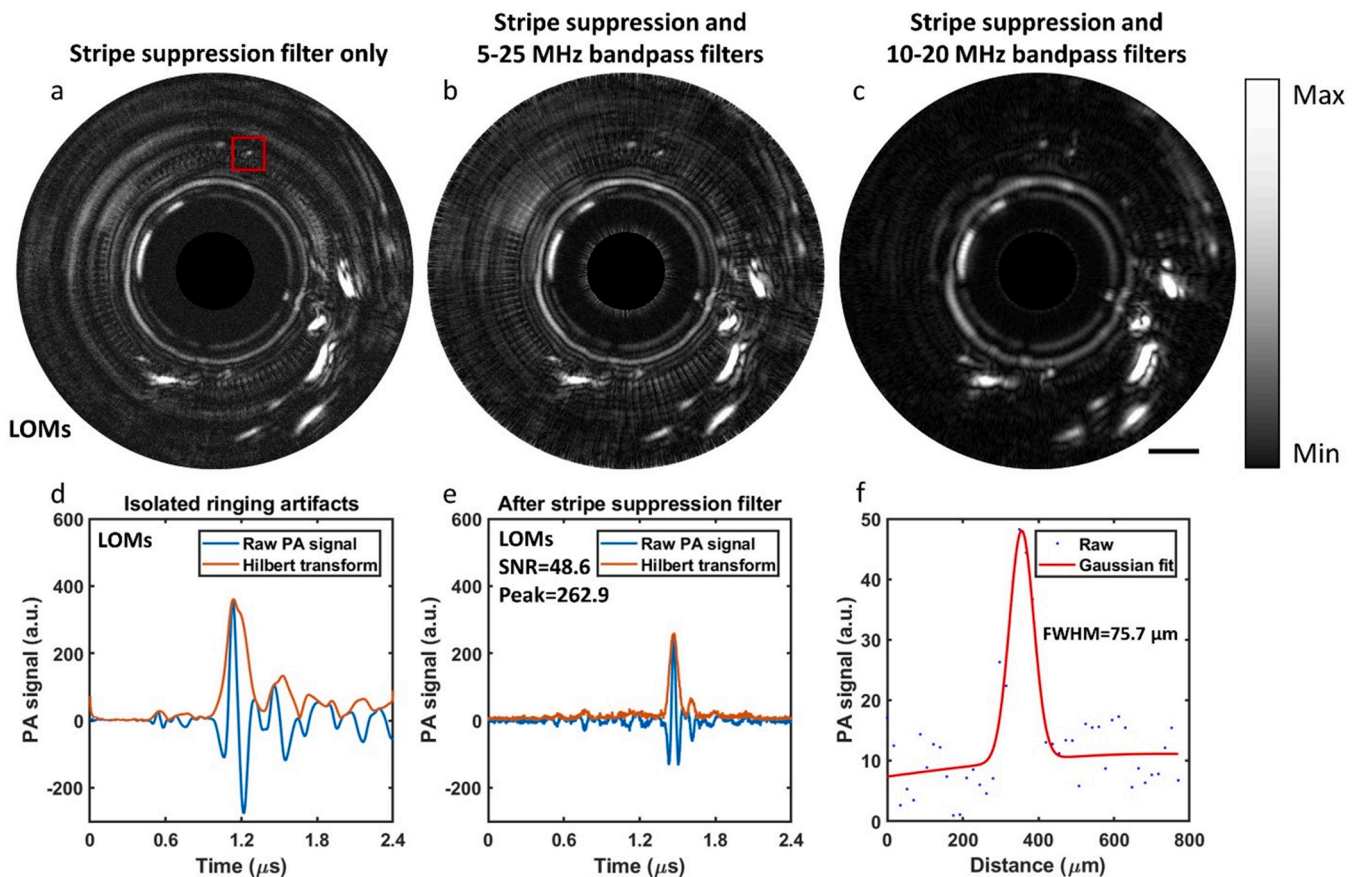
Fig. 5. High-sensitivity and high-spatial-resolution lipid detection through mode self-cleaning GRIN fiber and ringing artifact subtraction. (a-c) Same IVPA images in LOMs as in Fig. 3 after removing the ringing artifacts. Scale bar: 1 mm. (d) Isolated ringing artifacts in the same A-line (yellow dotted line in Fig. 3). (e) PA signals of lipid in the same A-line after removing the ringing artifacts. (f) FWHM = 75.7 μm for the small lipid signal in the red box in (a).

The suppression of ringing artifacts is necessary when imaging a relatively small artery like coronary arteries. Although removal of the ringing artifact by subtracting a background image has been reported [45], a proper way to remove the artifact in a single image has not been achieved. In this study, by converting the polar IVPA images into cartesian coordinates, ringing artifacts turned out to be stripes that occurred at certain time in certain laser modes. Filtering the stripy background was achieved with a stripe suppression filter.

5. Conclusions

We demonstrated a high-sensitivity and high-spatial-resolution intravascular photoacoustic catheter through mode cleaning in a graded-index multimode fiber. A nanosecond laser at wavelength of 1.7 μm was used for lipid excitation. The system was evaluated by imaging a phantom mimicking atherosclerotic plaque. The performance of LOMs and HOMs after a GRIN fiber for sensing lipids with a 10 MHz ultrasound transducer was compared. The SNR was 2.3 times improved by employing the mode self-cleaning effect. We also efficiently removed the dominant ringing artifacts with a stripe suppression filter. With these efforts, lipid particles as small as 75.7 μm in the phantom were clearly imaged.

Funding information

Declaration of Competing Interest

Ji-Xin Cheng declares a financial interest in Vibronix Inc, which does not support this work. Michael Sturek declares a financial interest in CorVus Biomedical, LLC, which does not support this work.

Data Availability

The datasets generated and analyzed during the current study are available from the corresponding author on reasonable request.

Appendix A. Supporting information

Supplementary data associated with this article can be found in the online version at doi:10.1016/j.pacs.2023.100451.

References

[1] P. Libby, The changing landscape of atherosclerosis, Nature 592 (7855) (2021) 524–533.
[2] Falk, E., V. Shah Pk Fau - Fuster, and V. Fuster, Coronary plaque disruption. (0009–7322 (Print)).
[3] L. Yao, J. Heuser-Baker, O. Herlea-Pana, R. Iida, Q. Wang, M.-H. Zou, J. Barlic-Dicen, Bone marrow endothelial progenitors augment atherosclerotic plaque regression in a mouse model of plasma lipid lowering, Stem Cells 30 (12) (2012) 2720–2731.
[4] K.J. Moore, F.J. Sheedy, E.A. Fisher, Macrophages in atherosclerosis: a dynamic balance, Nat. Rev. Immunol. 13 (10) (2013) 709–721.
[5] J.S. Lawton, J.E. Tamis-Holland, S. Bangalore, E.R. Bates, T.M. Beckie, J. M. Bischoff, J.A. Bittl, M.G. Cohen, J.M. DiMaio, C.W. Don, S.E. Fremes, M. F. Gaudino, Z.D. Goldberger, M.C. Grant, J.B. Jaswal, P.A. Kurlansky, R. Mehran, T. S. Metkus, L.C. Nnacheta, S.V. Rao, F.W. Sellke, G. Sharma, C.M. Yong, B. A. Zwischenberger, ACC/AHA/SCAI guideline for coronary artery

revascularization: a report of the American College of Cardiology/American Heart Association Joint Committee on Clinical Practice Guidelines, Circulation, 2022 145 (3) (2021) e18–e114.

[6] S.E. Nissen, E.M. Tuzcu, P. Schoenhagen, B.G. Brown, P. Ganz, R.A. Vogel, T. Crowe, G. Howard, C.J. Cooper, B. Brodie, Effect of intensive compared with moderate lipid-lowering therapy on progression of coronary atherosclerosis: a randomized controlled trial, JAMA 291 (9) (2004) 1071–1080.

[7] P. Libby P.M. Ridker A. Maseri *Inflamm. Atheroscler.* Circ. 105 9 2002 1135 1143.

[8] S.S. Virani, S.C. Smith, N.J. Stone, S.M. Grundy, Secondary prevention for atherosclerotic cardiovascular disease, Circulation 141 (14) (2020) 1121–1123.

[9] F. Gragnano, P. Calabrò, Role of dual lipid-lowering therapy in coronary atherosclerosis regression: Evidence from recent studies, Atherosclerosis 269 (2018) 219–228.

[10] Silva Marques, J. and F.J. Pinto, The vulnerable plaque: current concepts and future perspectives on coronary morphology, composition and wall stress imaging. (2174–2030 (Electronic)).

[11] P.J. de Feyter, P.W. Serruys, M.J. Davies, P. Richardson, J. Lubsen, M.F. Oliver, Quantitative coronary angiography to measure progression and regression of coronary atherosclerosis, *Value Limit. Implic. Clin. Trials* Circ. 84 (1) (1991) 412–423.

[12] G.S. Mintz, S.E. Nissen, W.D. Anderson, S.R. Bailey, R. Erbel, P.J. Fitzgerald, F. J. Pinto, K. Rosenfield, R.J. Siegel, E.M. Tuzcu, American College of Cardiology clinical expert consensus document on standards for acquisition, measurement and reporting of intravascular ultrasound studies (ivus) A report of the american college of cardiology task force on clinical expert consensus documents developed in collaboration with the european society of cardiology endorsed by the society of cardiac angiography and interventions, J. Am. Coll. Cardiol. 37 (5) (2001) 1478–1492.

[13] X. Li, J. Li, J. Jing, T. Ma, S. Liang, J. Zhang, D. Mohar, A. Raney, S. Mahon, M. Brenner, Integrated IVUS-OCT imaging for atherosclerotic plaque characterization, IEEE J. Sel. Top. Quantum Electron. 20 (2) (2013) 196–203.

[14] S. Brugaletta, H.M. Garcia-Garcia, P.W. Serruys, S. De Boer, J. Ligthart, J. Gomez-Lara, K. Witberg, R. Diletti, J. Wykrzykowska, R.-J. van Geuns, NIRS and IVUS for characterization of atherosclerosis in patients undergoing coronary angiography, JACC: Cardiovasc. Imaging 4 (6) (2011) 647–655.

[15] A. Kole, Y. Cao, J. Hui, I.A. Bolad, M. Alloosh, J.-X. Cheng, M. Sturek, Comparative quantification of arterial lipid by intravascular photoacoustic-ultrasound imaging and near-infrared spectroscopy-intravascular ultrasound, J. Cardiovasc. Transl. Res. 12 (3) (2019) 211–220.

[16] J. Bec, D.M. Ma, D.R. Yankelevich, J. Liu, W.T. Ferrier, J. Southard, L. Marcu, Multispectral fluorescence lifetime imaging system for intravascular diagnostics with ultrasound guidance: in vivo validation in swine arteries, Wiley Online Libr. (2014) 281–285.

[17] B. Wang, A. Karpiouk, D. Yeager, J. Amirian, S. Litovsky, R. Smalling, S. Emelianov, In vivo intravascular ultrasound-guided photoacoustic imaging of lipid in plaques using an animal model of atherosclerosis, Ultrasound Med. Biol. 38 (12) (2012) 2098–2103.

[18] K. Jansen, van Soest, A.F.W. van der Steen, Intravascular photoacoustic imaging: a new tool for vulnerable plaque identification, Ultrasound Med. Biol. 40 (6) (2014) 1037–1048.

[19] Y. Cao, J. Hui, A. Kole, P. Wang, Q. Yu, W. Chen, M. Sturek, J.-X. Cheng, High-sensitivity intravascular photoacoustic imaging of lipid–laden plaque with a collinear catheter design, Sci. Rep. 6 (1) (2016) 25236.

[20] J. Hui, Y. Cao, Y. Zhang, A. Kole, P. Wang, G. Yu, G. Eakins, M. Sturek, W. Chen, J.-X. Cheng, Real-time intravascular photoacoustic-ultrasound imaging of lipid-laden plaque in human coronary artery at 16 frames per second, Sci. Rep. 7 (1) (2017) 1417.

[21] P. Wang, T. Ma, M.N. Slipchenko, S. Liang, J. Hui, K.K. Shung, S. Roy, M. Sturek, Q. Zhou, Z. Chen, J.-X. Cheng, High-speed Intravascular Photoacoustic Imaging of Lipid-laden Atherosclerotic Plaque Enabled by a 2-kHz Barium Nitrite Raman Laser, Sci. Rep. 4 (1) (2014) 6889.

[22] Y. Cao, A. Kole, L. Lan, P. Wang, J. Hui, M. Sturek, J.-X. Cheng, Spectral analysis assisted photoacoustic imaging for lipid composition differentiation, Photoacoustics 7 (2017) 12–19.

[23] Y. Zhang, E. Taylor, N. Huang, J. Hamilton, J.-X. Cheng, Survival intravascular photoacoustic imaging of lipid-rich plaque in cholesterol fed rabbits, Transl. Biophotonics (2022) e202200012.

[24] Y. Cao, M. Alloosh, M. Sturek, J.-X. Cheng, Highly sensitive lipid detection and localization in atherosclerotic plaque with a dual-frequency intravascular photoacoustic/ultrasound catheter, Transl. Biophotonics 2 (3) (2020) e202000004.

[25] B. Wang, J.L. Su, J. Amirian, S.H. Litovsky, R. Smalling, S. Emelianov, Detection of lipid in atherosclerotic vessels using ultrasound-guided spectroscopic intravascular photoacoustic imaging, Opt. Express 18 (5) (2010) 4889–4897.

[26] B.K. Andrei, W. Bo, Y.E. Stanislav, H.A.M.D. James, W.S.M.D. Richard, Feasibility of in vivo intravascular photoacoustic imaging using integrated ultrasound and photoacoustic imaging catheter, J. Biomed. Opt. 17 (9) (2012), 096008.

[27] Z. Xie, C. Shu, D. Yang, H. Chen, C. Chen, G. Dai, K.H. Lam, J. Zhang, X. Wang, Z. Sheng, D. Gao, C. Liu, L. Song, X. Gong, In vivo intravascular photoacoustic imaging at a high speed of 100 frames per second, Biomed. Opt. Express 11 (11) (2020) 6721–6731.

[28] Hui, J. and J.-X. Cheng, Intravascular Photoacoustic Imaging of Lipid-Laden Plaques: From Fundamental Concept Toward Clinical Translation, in Multimodality Imaging: For Intravascular Application, Q. Zhou and Z. Chen, Editors. 2020, Springer Singapore: Singapore. p. 81–104.

[29] B. Wang, A. Karpiouk, D. Yeager, J. Amirian, S. Litovsky, R. Smalling, S. Emelianov, Intravascular photoacoustic imaging of lipid in atherosclerotic plaques in the presence of luminal blood, Opt. Lett. 37 (7) (2012) 1244–1246.

[30] J. Hui, Q. Yu, T. Ma, P. Wang, Y. Cao, R.S. Bruning, Y. Qu, Z. Chen, Q. Zhou, M. Sturek, J.-X. Cheng, W. Chen, High-speed intravascular photoacoustic imaging at 1.7 μm with a KTP-based OPO, Biomed. Opt. Express 6 (11) (2015) 4557–4566.

[31] Z. Piao, T. Ma, J. Li, M.T. Wiedmann, S. Huang, M. Yu, K. Kirk Shung, Q. Zhou, C.-S. Kim, Z. Chen, High speed intravascular photoacoustic imaging with fast optical parametric oscillator laser at 1.7 μm, Appl. Phys. Lett. 107 (8) (2015), 083701.

[32] B. Wang, E. Yantsen, T. Larson, A.B. Karpiouk, S. Sethuraman, J.L. Su, K. Sokolov, S.Y. Emelianov, Plasmonic intravascular photoacoustic imaging for detection of macrophages in atherosclerotic plaques, Nano Lett. 9 (6) (2009) 2212–2217.

[33] L. Lin, Z. Xie, M. Xu, Y. Wang, S. Li, N. Yang, X. Gong, P. Liang, X. Zhang, L. Song, F. Cao, IVUS\IVPA hybrid intravascular molecular imaging of angiogenesis in atherosclerotic plaques via RGDfk peptide-targeted nanoprobes, Photoacoustics 22 (2021), 100262.

[34] X. Bai, X. Gong, W. Hau, R. Lin, J. Zheng, C. Liu, C. Zeng, X. Zou, H. Zheng, L. Song, Intravascular optical-resolution photoacoustic tomography with a 1.1 mm diameter catheter, PLoS One 9 (3) (2014), e92463.

[35] L. Wang, P. Lei, X. Wen, P. Zhang, S. Yang, Tapered fiber-based intravascular photoacoustic endoscopy for high-resolution and deep-penetration imaging of lipid-rich plaque, Opt. Express 27 (9) (2019) 12832–12840.

[36] M. Fujiwara, K. Toubaru, S. Takeuchi, Optical transmittance degradation in tapered fibers, Opt. Express 19 (9) (2011) 8596–8601.

[37] J. Zhou, J.V. Jokerst, Photoacoustic imaging with fiber optic technology: a review, Photoacoustics 20 (2020), 100211.

[38] Y. Li, Z. Chen, Multimodal Intravascular Photoacoustic and Ultrasound Imaging, Biomed. Eng. Lett. 8 (2) (2018) 193–201.

[39] K. Krupa, A. Tonello, B.M. Shalaby, M. Fabert, A. Barthélémy, G. Millot, S. Wabnitz, V. Couderc, Spatial beam self-cleaning in multimode fibres, Nat. Photonics 11 (4) (2017) 237–241.

[40] Y. Zhang, Y. Cao, J.-X. Cheng, High-resolution photoacoustic endoscope through beam self-cleaning in a graded index fiber, Opt. Lett. 44 (15) (2019) 3841–3844.

[41] L.G. Wright, D.N. Christodoulides, F.W. Wise, Controllable spatiotemporal nonlinear effects in multimode fibres, Nat. Photonics 9 (5) (2015) 306–310.

[42] C.A. Schneider, W.S. Rasband, K.W. Eliceiri, NIH Image to ImageJ: 25 years of image analysis, Nat. Methods 9 (7) (2012) 671–675.

[43] A. Mafi, Pulse propagation in a short nonlinear graded-index multimode optical fiber, J. Lightw. Technol. 30 (17) (2012) 2803–2811.

[44] M. Xu, L.V. Wang, Photoacoustic imaging in biomedicine, Rev. Sci. Instrum. 77 (4) (2006), 041101.

[45] K. Jansen, M. Wu, A.F.W. van der Steen, G. van Soest, Photoacoustic imaging of human coronary atherosclerosis in two spectral bands, Photoacoustics 2 (1) (2014) 12–20.

Yuhao Yuan is currently a Postdoctoral Associate in the Department of Electrical and Computer Engineering at Boston University. He received his BSc degree in Basic Medical Sciences at Southern Medical University (Guangzhou, China) in 2017 and his Ph.D. degree in Biomedical Engineering at Binghamton University, State University of New York, in 2022. He joined Cheng Lab at Boston University as a Postdoctoral Associate in fall 2022. His research interests include photoacoustic imaging and coherent Raman imaging.

Guangju Zhang received his BS degree at School of Optoelectronic Engineering, Changchun University of Science and Technology in 2012 (Changchun, China), his MS degree at Institute of Laser Engineering, Beijing University of Technology in 2015 (Beijing, China) and his Ph.D degree at Department of Precision Instrument, Tsinghua University in 2019 (Beijing, China). He worked as a postdoctoral associate at Department of Bioengineering, University of Washington in 2019–2020. In 2020, he joined Cheng Lab at Department of Electrical and Computer Engineering, Boston University as a postdoctoral associate. His research interests include solid-state and fiber lasers, pulsed lasers, 2-D materials, optical coherence tomography and photoacoustics.

Yuqi Chen is currently an M.S. student in the Department of Biomedical Engineering at Boston University. She received her B.Eng. in Biomedical Engineering in 2020 at Shenzhen University. Her research focuses on fast photoacoustic imaging.

Hongli Ni is a Ph.D. student in the Department of Electrical and Computer Engineering at Boston University. She received her Bachelor's degree in Optical Science and Engineering at Zhejiang University (Hangzhou, China) in 2019. She joined the Cheng group at Boston University in 2019. Her research interests include coherent Raman imaging and clinical translation of label-free chemical imaging.

Mingsheng Li is currently a Ph.D. candidate in the Department of Electrical and Computer Engineering at Boston University. He received his BSc degree in Tsinghua University (Beijing, China) in 2018. His research interests include photoacoustic and photothermal imaging.

Michael Sturek received his B.A. from Augustana College, M. S. from Purdue University, Ph.D. from the University of Iowa, and did postdoctoral training at the University of Chicago. He was on faculty at the University of Missouri as Director of Basic Research in the Center for Diabetes & Cardiovascular Disease. Sturek was Chair of the Department of Cellular & Integrative Physiology at Indiana University School of Medicine for 15 years. He was Professor at Indiana, an Adjunct Professor of Biomedical Engineering at Purdue University, and is currently Chief Scientific Officer at CorVus Biomedical, LLC and non-profit CorVus Foundation, Inc. His research program focuses on vascular imaging ranging from cellular Ca^{2+} dynamics to intravascular ultrasound, photoacoustic, and positron emission tomography of atherosclerosis and vascular calcification.

Ji-Xin Cheng is currently the Moustakas Chair Professor in Photonics and Optoelectronics at Boston University. Cheng joined Purdue University in 2003 as Assistant Professor in Weldon School of Biomedical Engineering and Department of Chemistry, promoted to Associate Professor in 2009 and Full Professor in 2013. He joined Boston University as the Inaugural Theodore Moustakas Chair Professor in Photonics and Optoelectronics in summer 2017. His research lab at Boston focuses on developing and applying molecular spectroscopic imaging and cell modulation technologies to enable discovery-driven research towards marker-based precise diagnosis and/or treatment of human diseases.